mater.scichina.com link.springer.com

Published online 2 April 2021 | https://doi.org/10.1007/s40843-020-1625-2
Sci China Mater 2021, 64(8): 1858–1867

Photo-stable perovskite solar cells with reduced interfacial recombination losses using a CeO_x interlayer

Xiaoqiang Shi[1], Ye Tao[1], Zhuoxin Li[1], Huirong Peng[1], Molang Cai[1,2*], Xuepeng Liu[1], Zhongyan Zhang[1] and Songyuan Dai[1,2*]

ABSTRACT **Despite demonstrating remarkable power conversion efficiencies (PCEs), perovskite solar cells (PSCs) have not yet achieved their full potential. In particular, the interfaces between the perovskite and charge transport layers account for the vast majority of the recombination losses. Interfacial contact and band alignment between the low-temperature-processed TiO_2 electron transport layer (ETL) and the perovskite are essential to minimize nonradiative recombination losses. In this study, a CeO_x interlayer is employed to modify the perovskite/TiO_2 interface, and the charge transport properties of the devices are investigated. The bilayer-structured TiO_2/CeO_x ETL leads to the modification of the interface energetics, resulting in improved electron extraction and reduced nonradiative recombination in the PSCs. Devices based on TiO_2/CeO_x ETL exhibit a high open-circuit voltage (V_{oc}) of 1.13 V and an enhanced PCE of more than 20% as compared with V_{oc} of 1.08 V and a PCE of approximately 18% for TiO_2-based devices. Moreover, PSCs based on TiO_2/CeO_x ETL maintain over 88% of their initial PCEs after light illumination for 300 min, whereas PSCs based on TiO_2 ETL almost failed. This study provides an efficient strategy to enhance the PCE and stability of PSCs based on a low-temperature-processed TiO_2 ETL.**

Keywords: perovskite solar cell, interface passivation, recombination, light stability, CeO_x

INTRODUCTION

In the past decade, huge efforts have been devoted worldwide to understanding and improving the performance of perovskite solar cells (PSCs), which already outperform other conventional thin-film photovoltaic technologies [1–5]. Recently, the highest certified power conversion efficiency (PCE) of PSCs has reached 25.5% [6]. It is well established that further improvements in the performance of PSCs will require suppression of nonradiative charge recombination (trap-assisted charge recombination) losses to unlock the full thermodynamic potential of PSCs [7–9]. Charge transport layers (CTLs) are key components of high-performance PSCs; however, interface defects and energy level misalignments can induce additional nonradiative recombination pathways, which limit the open-circuit voltage (V_{oc}) and fill factor (FF) of PSCs. CTLs/perovskite interfaces dominate the nonradiative recombination in efficient PSCs [9]. Therefore, to realize the full thermodynamic potential of the perovskite absorber, the formation of a good contact for the CTLs/perovskite interface is essential.

The addition of interlayers between the CTLs and perovskite absorber has proven to be an efficient method to mitigate interfacial recombination losses [10–12]. For the interface between the electron transport layer (ETL) and perovskite, a broad range of interlayer materials, including metal oxides, conjugated polymers, small molecules, and fullerenes, has been reported [13–15]. Among these, metal-oxide interlayers are frequently used in PSCs owing to their good chemical stability, which endows the interlayers with robust (solvent-resistant) properties [16–20]. TiO_2 films annealed under high temperature are widely employed as the ETL, with the aim of achieving high-performance PSCs. However, low-temperature-processed TiO_2-based planar PSCs exhibit low efficiencies due to intrinsic problems such as the unsuitable conduction band energy and low electron extraction ability of

[1] Beijing Key Laboratory of Novel Thin-Film Solar Cells, North China Electric Power University, Beijing 102206, China
[2] State Key Laboratory of Alternate Electrical Power System with Renewable Energy Sources, North China Electric Power University, Beijing 102206, China
* Corresponding authors (emails: molangcai@ncepu.edu.cn (Cai M); sydai@ncepu.edu.cn (Dai S))

TiO_2. Several attempts have been made at modifying the TiO_2 ETL in planar PSCs using metal-oxide interlayers to reduce the interface recombination losses. For instance, the insertion of a ZnO interlayer between the TiO_2 layer and perovskite reduces interfacial recombination due to the proper energy alignment [21,22]. Thermal instability has been observed in ZnO-based PSCs and is attributed to the deprotonation of the organic cation caused by the basic nature of the ZnO surface [23]. Moreover, an enhanced charge extraction ability and suppressed carrier recombination at the TiO_2/perovskite interface were also achieved using SnO_2 as the interlayer [24,25]. In addition to interfacial charge recombination, another issue associated with TiO_2-based PSCs is the photo-induced device degradation [26]. These problems stimulate further research toward exploring efficient ETLs with favored interface contact and good light stability.

Here, we propose an ETL comprising an amorphous CeO_x interlayer on top of a TiO_2 compact layer fabricated *via* a low-temperature solution process. Furthermore, we perform a comprehensive study on planar PSCs based on the TiO_2/CeO_x double layer. It is shown that the band alignment, electron extraction, PCE, hysteresis, and stability of PSCs can be significantly improved using the bilayer-structured TiO_2/CeO_x ETL compared with the pure TiO_2 ETL. Owing to the reduced interfacial charge recombination, solar cells based on the TiO_2/CeO_x ETL demonstrate a maximum V_{oc} of 1.13 V with 300 mV potential loss compared with the TiO_2-based cell (1.08 V and 520 mV, respectively). The enhancement of V_{oc}, together with the increase in FF (from ~74% to ~76%), enables a PCE improvement from ~18% to more than 20%. Moreover, thanks to the presence of the CeO_x interlayer, the PSCs exhibit a significantly improved light stability.

EXPERIMENTAL SECTION

Materials

Fluorine-doped tin-oxide (FTO) glasses (≤15 Ω sq^{-1}) were purchased from South China Science & Technology Company Limited. Titanium(IV) chloride ($TiCl_4$) and titanium diisopropoxide bis(acetylacetonate) were obtained from Sigma-Aldrich. Cerium(III) acetylacetonate hydrate was purchased from 9 Ding Chemistry. Methylammonium iodide (MAI) and lead(II) iodide (PbI_2) were purchased from TCI. 2,2′,7,7′-Tetrakis-(*N*,*N*-di-*p*-methoxyphenylamine)9,9′-spirobifluorene (Spiro-OMeTAD), 4-*tert*-butylpyridine (*t*BP), lithium bis(trifluoromethanesulfonyl)imide (Li-TFSI), and tris(2-(1H-pyrazol-1-yl)-4-tert-butylpyridine)-cobalt(III) tris(bis(trifluoromethylsulfonyl)imide) (FK209) were purchased from Xi'an Polymer Light Technology Corp. Anhydrous solvents, such as dimethylformamide (DMF), dimethyl sulfoxide (DMSO), chlorobenzene, ethanol, benzyl alcohol, diethyl ether, isopropanol, and acetonitrile were obtained from Alfa Aesar. All the chemicals were used as received without further purification.

Device fabrication

The pre-patterned FTO substrates were sequentially cleaned with saturated sodium hydroxide ethanol solution, deionized water, and ethanol and then exposed to UV–ozone for 15 min. For the TiO_2 ETL, 100 μL of the colloidal TiO_2 nanocrystal solution was spin-coated onto the FTO substrate and annealed on a hot plate at 150°C for 30 min in ambient air. For the CeO_x interlayer, 100 μL of the precursor solution was spin-coated onto the TiO_2 substrate and annealed at 150°C for 30 min. All ETLs were exposed to UV–ozone for 15 min prior to the deposition of the active layer. The perovskite layer was prepared from a precursor solution containing 1.4 mol L^{-1} of $MAPbI_3$ in a mixed solvent of DMF and DMSO, with the volume ratio of DMF to DMSO being 1:4. The perovskite precursor solution was spin-coated onto different substrates *via* a consecutive two-step spin-coating process, at 1200 and 4200 rpm for 10 and 30 s, respectively. During the second step, 120 μL of chlorobenzene was poured onto the spinning substrate 10 s prior to the end of the spinning process. The films were then annealed on a hotplate at 100°C for 15 min. Once being cooled to room temperature, Spiro-OMeTAD was deposited on top of the perovskite layer *via* spin-coating at 4000 rpm for 30 s. The Spiro-OMeTAD solution was prepared by dissolving 73.53 mg (60 mmol L^{-1}) of Spiro-OMeTAD in 1 mL of chlorobenzene, with the addition of 29.30 μL (200 mmol L^{-1}) of *t*BP and 17.23 μL (30 mmol L^{-1}) of Li-TFSI solution (500 mg Li-TFSI in 1 mL acetonitrile). Next, 6.78 μL (1.8 mmol L^{-1}) of FK209 solution (400 mg FK209 in 1 mL acetonitrile) was added to the Spiro-OMeTAD solution; the molar ratio for FK209 and Spiro-OMeTAD was 0.03. Finally, an 80-nm gold layer was thermally evaporated on top of the device.

Characterizations

The morphology and crystal structure of the perovskite films were characterized *via* scanning electron microscopy (SEM, SU8010, Hitachi) and X-ray diffraction (XRD, Smartlab SE, Rigaku), respectively. The absorption spectra of the perovskite films were measured using a

UV–Vis spectrometer (UV-3600Plus, Shimadzu). X-ray photoelectron spectroscopy (XPS) and ultraviolet photoelectron spectroscopy (UPS) were performed using a multifunctional photoelectron spectrometer (ESCALAB 250Xi, Thermo Scientific). Steady-state photoluminescence (PL) was performed using a home-built system. Current density–voltage (J–V) curves were recorded using a Keithley 2400 source meter under simulated sunlight from a Newport AAA solar simulator.

RESULTS AND DISCUSSION

Preparation of the low-temperature solution-processed TiO_2 and TiO_2/CeO_x ETLs is shown schematically in Fig. 1a. The TiO_2 nanocrystals were synthesized following a modified nonhydrolytic sol–gel method [27], whereas the CeO_x precursor solution was obtained by dissolving cerium(III) acetylacetonate hydrate in ethanol. All experimental details are provided in the experimental section. The surface and cross-sectional morphologies of the TiO_2 and TiO_2/CeO_x ETLs are shown in Fig. 1b–e. As can be seen from Fig. 1b, c, negligible difference can be observed between the surface topographies of the TiO_2 and TiO_2/CeO_x ETLs, indicating the presence of an ultra-thin CeO_x interlayer. To confirm this, the SEM image of the FTO/CeO_x film is shown in Fig. S1. The morphology of the FTO polycrystalline layer can be clearly distinguished after being covered with a thin CeO_x layer, in agreement with previous study [28]. XRD patterns show negligible difference between the TiO_2 and TiO_2/CeO_x films (Fig. S2), indicating that the low-temperature solution-processed CeO_x interlayer is amorphous. From the cross-sectional view (Fig. 1d, e), it can be seen that the surface roughness of the FTO/TiO_2 film reduced after the introduction of the CeO_x interlayer. Atomic force microscopy measurements were performed to understand the influence of the CeO_x interlayer on the surface roughness. As shown in Fig. S3, the TiO_2/CeO_x film exhibits a reduced root-mean-square (RMS) surface roughness (RMS = 19.2 nm) compared with that of the TiO_2 film (RMS = 16.1 nm), which is in good agreement with the SEM results.

To investigate the influence of the CeO_x interlayer on the morphology and crystallinity properties of perovskite films, SEM and XRD were conducted on the perovskite films deposited onto TiO_2 and TiO_2/CeO_x ETLs. As shown in Fig. 2a–d, the grain sizes and film thicknesses of

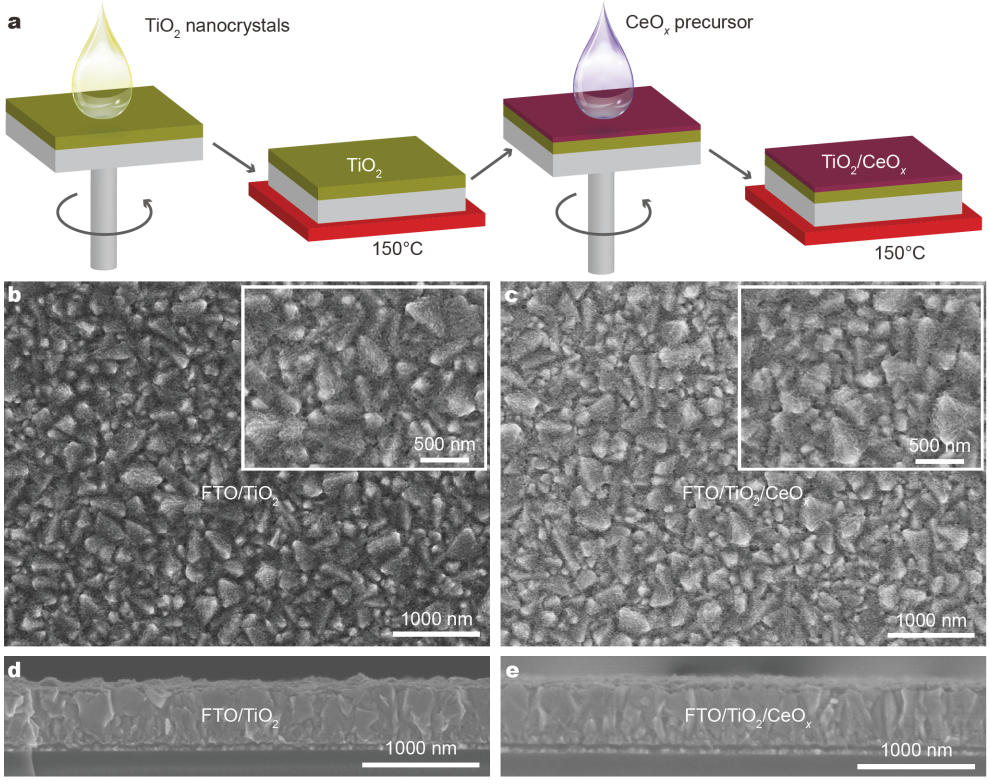

Figure 1 (a) Preparation of the low-temperature solution-processed TiO_2 and TiO_2/CeO_x films. (b, c) Surface SEM images of the TiO_2 and TiO_2/CeO_x films. The insets show the corresponding high-magnification SEM images. (d, e) Cross-sectional SEM images of the TiO_2 and TiO_2/CeO_x films.

the perovskite films deposited onto TiO_2 and TiO_2/CeO_x ETLs are similar. The perovskite film based on TiO_2/CeO_x ETL exhibits a slightly enhanced absorption compared with the perovskite film based on the TiO_2 ETL (Fig. 2e). Fig. 2f shows the XRD patterns of the perovskite films deposited onto the TiO_2 and TiO_2/CeO_x ETLs. The main peaks located at 14.1° and 28.5° correspond to the (110) and (220) crystal planes of the cubic perovskite phase, respectively [29]. The perovskite (110) peak intensity does not show any discernible difference between the two films. Analogously, the full-width-at-half-maximum values of this perovskite (110) peak are similar for the two films (0.12 for the TiO_2-based film and 0.11 for the TiO_2/CeO_x-based film). In addition, the ratio of the perovskite (110) peak intensity to the perovskite (220) peak intensity is 1.91 and 1.93 for the films deposited onto the TiO_2 and TiO_2/CeO_x ETLs, respectively. These results suggest that the introduction of the CeO_x interlayer has no significant effect on the morphologies and crystalline properties of the perovskite films.

XPS measurements were performed to confirm the presence of CeO_x interlayer and investigate its chemical composition. Fig. 3a shows the XPS survey for the TiO_2 and TiO_2/CeO_x films, whereas Fig. 3b illustrates the high-resolution Ce 3d core level spectra. An evident Ce 3d peak can be observed in the TiO_2/CeO_x film, whereas such a peak is absent in the spectra of the TiO_2 film. Fig. S4 shows the deconvolution of the Ce 3d core level XPS spectra for the TiO_2/CeO_x film. Both Ce^{3+} and Ce^{4+} emissions are present in the obtained CeO_x film. Regarding the spectrum of the fully oxidized CeO_2 film, six peaks can be identified, which correspond to three pairs of spin-orbit split doublets [30]. These peaks are labeled using conventional notations (U, U″, U‴, V, V″, and V‴). U and V refer to the $3d_{3/2}$ and $3d_{5/2}$ levels, respectively. The peaks labeled as U/V, U″/V″, and U‴/V‴ are assigned to a mixture of Ce $3d^9 4f^2$ O $2p^4$, Ce $3d^9 4f^1$ O $2p^5$, and Ce $3d^9 4f^0$ O $2p^6$, respectively. For the reduced ceria films, the spectra show two more pairs of doublets (indicated as U_0, U′, V_0, and V′), which originated from different Ce 4f configurations in the initial and final states associated with the Ce^{3+} ions. The peaks labeled as U_0/V_0 and U′/V′ are assigned to a mixture of Ce $3d^9 4f^2$ O $2p^5$ and Ce $3d^9 4f^1$ O $2p^6$, respectively. Therefore, the Ce 3d XPS region contains 10 peaks originating from different Ce oxidation states (Ce^{3+} and Ce^{4+}) and their 4f configurations. The component labeled U‴/V‴ is indicative of the Ce $3d^9 4f^0$ O $2p^6$ final state, which is associated with the presence of Ce^{4+} ions. The Ce^{3+} concentration in the Ce 3d spectrum is determined to be 0.46; therefore, the value of x in the as-prepared CeO_x is 1.77, which is in good agreement with previous studies [28,31]. It is worth noting that the presence of the TiO_2 support contributes to the increase in the Ce^{3+} concentration *via* interface stabilization [32–34]. Energy-dispersive spectroscopy mapping confirmed the uniform coverage of CeO_x on top of the TiO_2 film (Fig. S5). Due to the presence of the oxygen-deficient CeO_x layer, it can be inferred that charge

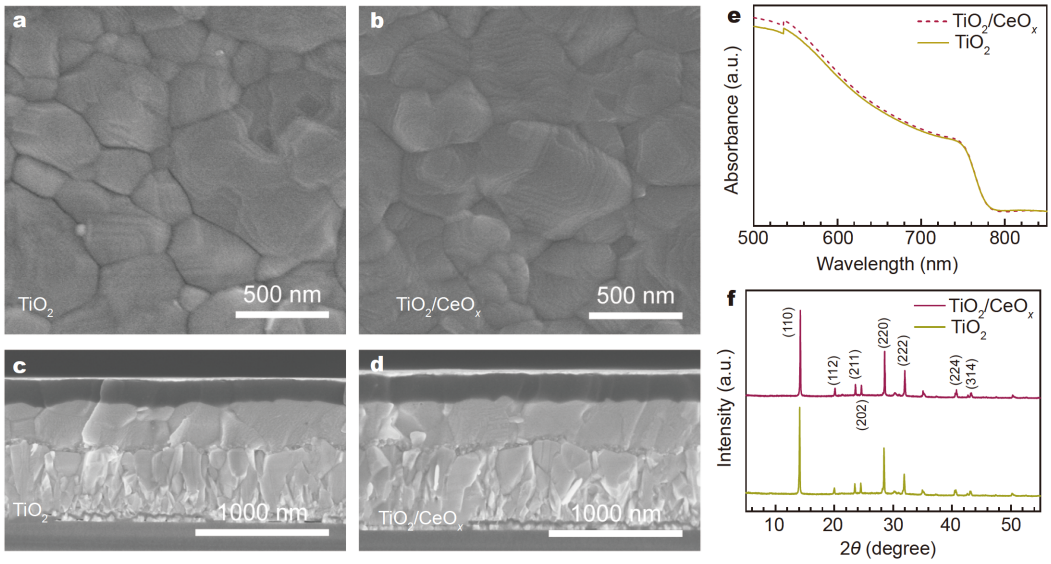

Figure 2 (a, b) Top-view SEM images of the perovskite films deposited onto the TiO_2 and TiO_2/CeO_x ETLs. (c, d) Cross-sectional view of the PSCs based on the TiO_2 and TiO_2/CeO_x ETLs. (e) UV–Vis absorption spectra of the perovskite films deposited onto the TiO_2 and TiO_2/CeO_x ETLs. (f) XRD patterns of the perovskite films deposited onto the TiO_2 and TiO_2/CeO_x ETLs.

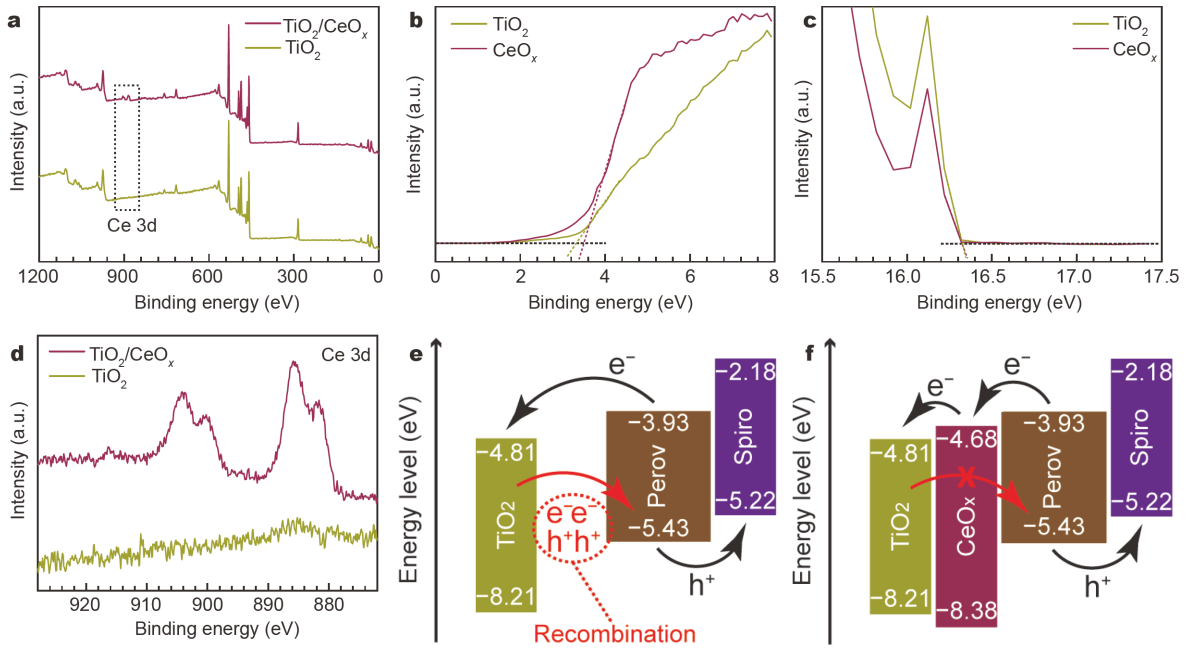

Figure 3 (a) XPS survey of the TiO_2 and TiO_2/CeO_x films. (b) Ce 3d core level spectra of the TiO_2 and TiO_2/CeO_x films. (c, d) Valence band spectra and secondary electron cut-off for the TiO_2 and CeO_x films. (e, f) Schematics of band alignment for the PSCs based on the TiO_2 and TiO_2/CeO_x ETLs.

recombination may occur at the CeO_x/perovskite interface. With this in mind, UV–ozone treatment was applied to remove surface oxygen vacancies and thus alleviate interface recombination [35,36].

Energy level matching between the perovskite layer and ETLs is critical for achieving high-performance PSCs. UPS measurements were performed to determine the energy level positions of the TiO_2 and CeO_x films. Fig. 3c, d show the valence band spectra and secondary electron cut-off for the TiO_2 and CeO_x films. According to the valence band spectra, the energy difference between the valence band maximum (VBM) and Fermi level was found to be ~3.33 and ~3.50 eV for the TiO_2 and CeO_x films, respectively. Additionally, the secondary electron cut-off is ~16.32 eV for both TiO_2 and CeO_x films, corresponding to a work function of 4.88 eV. Therefore, the VBMs for the TiO_2 and CeO_x films were estimated to be −8.21 and −8.38 eV, respectively. By combining VBM positions with optical bandgaps [27,31], the conduction band minimums (CBMs) were determined to be −4.81 and −4.68 eV for the TiO_2 and CeO_x films, respectively. Based on these values and reported band edges of $MAPbI_3$ and Spiro-OMeTAD [37], the energy band diagrams for the PSCs employing TiO_2 and TiO_2/CeO_x as ETLs were derived, as illustrated in Fig. 3e, f. Because the CBM of CeO_x lies between those of $MAPbI_3$ and TiO_2, photogenerated electrons in the conduction band of $MAPbI_3$ can cascade into TiO_2 *via* CeO_x. This optimally positioned band alignment facilitates the extraction of electrons from the perovskite and their subsequent injection into TiO_2. Additionally, CeO_x functions as a hole-blocking layer to suppress the electrons' back transfer from TiO_2 to the perovskite. The energy barrier at the TiO_2/CeO_x interface can effectively block charge recombination, which should essentially increase the quasi-Fermi level for electrons and raise the V_{oc} value.

To assess the influence of the CeO_x interlayer on the photovoltaic performance of PSCs, devices with the structure of FTO/ETLs/$MAPbI_3$/Spiro-OMeTAD/Au were assembled, as schematically illustrated in Fig. 4a. Fig. 4b shows the *J*–*V* curves (under reverse scan) for the PSCs based on the TiO_2 and TiO_2/CeO_x ETLs with the photovoltaic parameters summarized in Table 1. The TiO_2-based device exhibits a PCE of 18.61%, with a short-circuit current density (J_{sc}) of 23.18 mA cm^{-2}, V_{oc} of 1.08 V, and FF of 74.64%. Upon introducing the CeO_x interlayer, no obvious change is observed in the J_{sc} value (23.14 mA cm^{-2}); however, V_{oc} and FF increase to 1.13 V and 76.39%, respectively, yielding a promising PCE of more than 20%. Fig. 4c presents a statistical comparison of the averaged PCE from 36 individual devices with the TiO_2 and TiO_2/CeO_x ETLs. Compared with the TiO_2-based devices (17.27% ± 0.65%), the TiO_2/CeO_x devices exhibit an improvement in the averaged PCE (19.17% ±

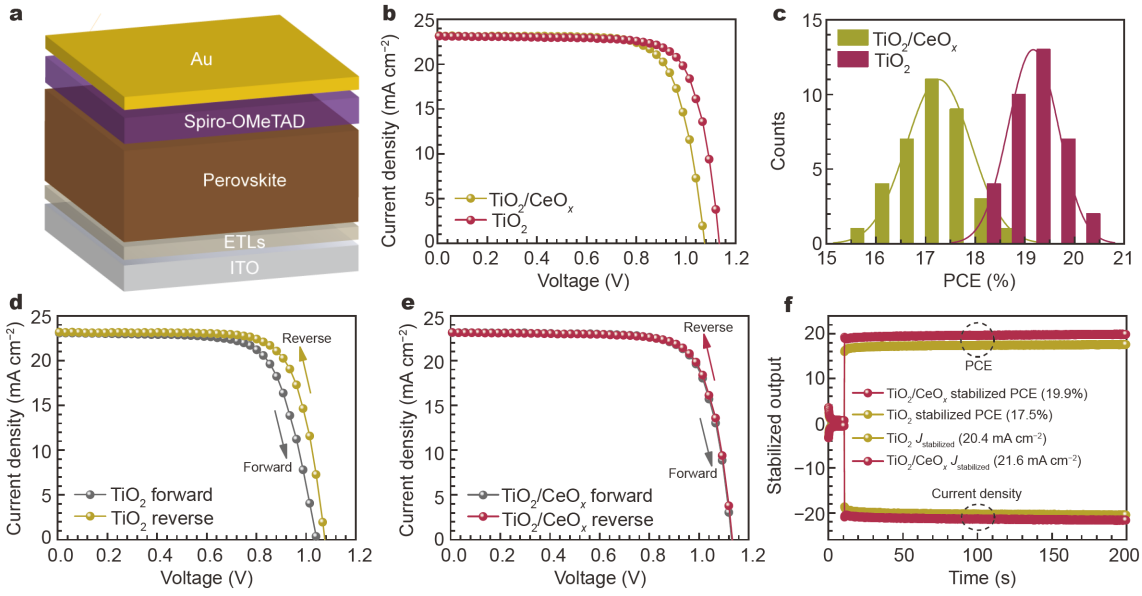

Figure 4 (a) Device configuration. (b) *J*–*V* curves of the PSCs based on the TiO_2 and TiO_2/CeO_x ETLs. (c) PCE distributions of the PSCs based on the TiO_2 and TiO_2/CeO_x ETLs. (d) *J*–*V* curves of the PSC based on the TiO_2 ETL under both reverse- and forward-scan directions. (e) *J*–*V* curves of the PSC based on the TiO_2/CeO_x ETL under both reverse- and forward-scan directions. (f) Steady-state power output of the PSCs based on the TiO_2 and TiO_2/CeO_x ETLs.

Table 1 Photovoltaic parameters of the PSCs based on the TiO_2 and TiO_2/CeO_x ETLs

Devices	Scan direction	J_{sc} (mA cm^{-2})	V_{oc} (V)	FF (%)	PCE (%)	HI (%)
TiO_2	Reverse	23.18	1.08	74.64	18.61	9.0
	Forward	23.08	1.04	70.91	17.07	
TiO_2/CeO_x	Reverse	23.14	1.13	76.39	20.05	0.6
	Forward	23.15	1.13	76.09	19.94	

0.50%) with a narrower PCE distribution. This further confirms the enhanced photovoltaic performance and reproducibility that can be obtained with the introduction of the CeO_x interlayer.

Fig. 4d, e show the *J*–*V* curves measured under both reverse and forward scans. The corresponding photovoltaic parameters are listed in Table 1. It was found that the TiO_2/CeO_x-based device shows negligible hysteresis, whereas the pure TiO_2-based device exhibits large hysteresis. To quantify the variation in the hysteresis behavior, the hysteresis index (HI) was calculated [37]. The HI decreased from 9.0% (TiO_2-based device) to 0.6% (TiO_2/CeO_x-based device), which can be ascribed to the improved electron extraction. Steady-state power output under continuous illumination can provide a more accurate and reliable photovoltaic performance for the devices under working conditions. Fig. 4f shows the steady-state PCE and current density measured at maximum power point. The PCEs for the PSCs based on TiO_2 and TiO_2/CeO_x ETLs stabilize at 17.5% and 19.9% with photocurrent densities of 20.4 and 21.6 mA cm^{-2}, respectively. It should be noted that these values are very close to those obtained from the *J*–*V* measurements.

Compared with the PSCs using TiO_2 as the ETL, a higher V_{oc} value is obtained when TiO_2/CeO_x is used as the ETL. When a solar cell is under illumination, the V_{oc} is related to the splitting of quasi-Fermi levels for electrons and holes. These quasi-Fermi level positions are set by the free-carrier concentration, which in turn is determined by the equilibrium between carrier generation and recombination rates [38,39]. For PSCs based on different ETLs, the carrier generation process is identical, and the enhanced V_{oc} observed in the TiO_2/CeO_x-based devices indicates a suppressed recombination of carriers either in the perovskite bulk or at the ETLs/perovskite interface. Considering the similar qualities of the perovskite films deposited onto TiO_2 and TiO_2/CeO_x ETLs (see Fig. 2), the enhancement of V_{oc} can be ascribed to the suppressed interfacial carrier recombination obtained due to the addition of the CeO_x interlayer. To understand the carrier recombination process in the PSCs, the *J*–*V* characteristics were analyzed based on the equivalent circuit model. Generally, the *J*–*V* characteristics of a semiconductor junction can be described as follows

[37,40]:

$$-\frac{dV}{dJ} = \frac{mk_BT}{q}(J_{sc} - J)^{-1} + R_s,$$

where m is the ideality factor, k_B is the Boltzmann constant, T is the temperature, q is the electron charge, J_{sc} is the photo-induced current density, and R_s is the series resistance. The value of m can be obtained by fitting the linear part of the $-dV/dJ$ *vs.* $(J_{sc} - J)^{-1}$ curves, as shown in Fig. 5a. The TiO_2/CeO_x-based device exhibits a decreased m value (2.23) compared with the TiO_2-based device (2.62). Generally, lower m value indicates a smaller probability for charge carrier recombination in PSCs [41]. Therefore, the reduced m value suggests a suppressed nonradiative carrier recombination in the TiO_2/CeO_x-based PSCs.

To further elucidate the improved optoelectronic quality and understand the carrier recombination process in PSCs with different ETLs, light intensity (φ)-dependent V_{oc} characteristics were measured, as shown in Fig. 5b [3]. The relationship between V_{oc} and φ can be described as $V_{oc} = \alpha(k_BT/q)\ln\varphi$, where α is a constant [42]. Assuming a homogeneous carrier profile in the PSCs, for a trap-free bimolecular recombination, α should be close to 1. On the contrary, if trap-assisted monomolecular recombination (mainly Shockley–Read–Hall recombination) dominates, α approaches 2. Thus, the deviation of α from 1 indicates the occurrence of nonradiative trap-assisted carrier recombination in the PSCs. The control device without the CeO_x interlayer exhibited a slope of $1.71k_BT/q$, suggesting a severe nonradiative loss due to trap-assisted recombination. A slope of $1.46k_BT/q$ was achieved when the TiO_2/perovskite interface was modified with the addition of CeO_x. This proves the role of CeO_x in reducing the interfacial nonradiative recombination in PSCs. V_{oc} decay measurements were conducted to investigate the transient process of carrier recombination in PSCs. Fig. 5c illustrates the V_{oc} decay curves of the PSCs with or without the CeO_x interlayer. It can be seen that the PSCs with the CeO_x interlayer exhibited a slower decay rate and longer decay time than the cells without the CeO_x interlayer. The V_{oc} decay time constant for the TiO_2/CeO_x-based device (2.16 ms) was estimated to be twice as large as that for the TiO_2-based device (1.03 ms). This result suggests that the PSCs that use the CeO_x interlayer possess a much longer carrier lifetime and lower interface recombination rate than the cells without the CeO_x interlayer; this is in consistent with the observed high V_{oc} and FF values of the devices with CeO_x. The electron lifetime (τ_n) can be derived from Fig. 5c on the basis of the following equation [43]:

$$\tau_n = -\frac{k_BT}{q}\left(\frac{dV_{oc}}{dt}\right)^{-1}.$$

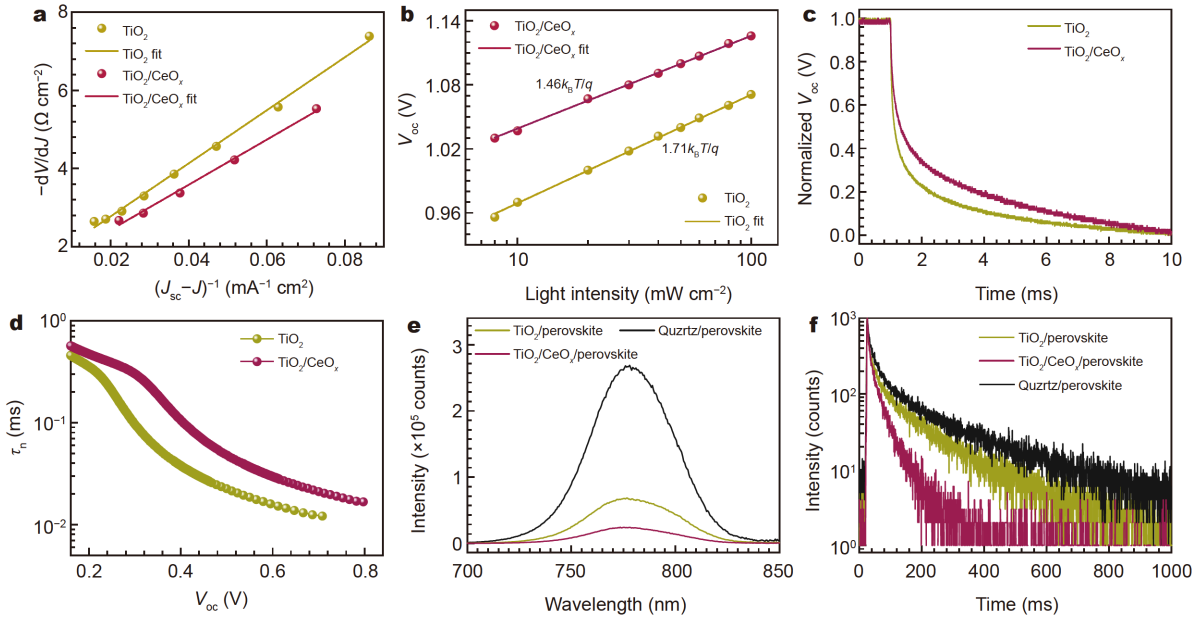

Figure 5 (a) Plots of $-dV/dJ$ *vs.* $(J_{sc} - J)^{-1}$ for the PSCs based on the TiO_2 and TiO_2/CeO_x ETLs and corresponding linear fittings. (b) V_{oc} *vs.* light intensity for the PSCs based on the TiO_2 and TiO_2/CeO_x ETLs and corresponding linear fittings. (c) V_{oc} decay curves for the PSCs based on the TiO_2 and TiO_2/CeO_x ETLs. (d) Calculated electron lifetimes for the PSCs based on the TiO_2 and TiO_2/CeO_x ETLs. (e, f) Steady-state PL spectra and TRPL decays of the perovskite films depositied onto quartz, TiO_2, and TiO_2/CeO_x substrates.

The dependence of τ_n on V_{oc} is shown in Fig. 5d; it can be seen that the TiO_2/CeO_x-based device exhibits longer τ_n than the TiO_2-based cell.

Steady-state PL measurements were conducted to study the charge transfer process between the perovskite and ETLs. Fig. 5e shows the PL spectra of perovskite films deposited onto different ETLs. A more strongly quenched PL was observed for the perovskite films based on the TiO_2/CeO_x ETL. This result suggests that electron extraction from the perovskite is more efficient for the TiO_2/CeO_x ETL; this is consistent with the improved energy level matching between the perovskite and the TiO_2/CeO_x ETL. Time-resolved PL (TRPL) measurements were performed to explore the dynamic recombination behavior of perovskite films prepared on different ETLs, as shown in Fig. 5f and Table S1. The TRPL decay curves were fitted using the biexponential equation, $I(t) = I_0 + A_1\exp(-t/\tau_1) + A_2\exp(-t/\tau_2)$, where τ_1 and τ_2 represent the fast and slow decay time constants, respectively. In general, τ_1 and τ_2 are associated with the quenching of charge carriers by electron extraction from the perovskite to ETLs and nonradiative recombination in the perovskite bulk, respectively [37]. The TiO_2 ETL-loaded perovskite exhibited a PL decay time of τ_1 = 15.1 ns and τ_2 = 139.9 ns, which are obviously slower than that of pure perovskite (Table S1). For the TiO_2/CeO_x ETL-loaded perovskite, both τ_1 and τ_2 decreased to 6.1 and 39.7 ns, respectively, suggesting an enhanced electron extraction between the perovskite and the TiO_2/CeO_x ETL. This is also confirmed by the reduced average lifetime from 107.8 to 31.0 ns. The enhanced electron extraction might originate from the improved band alignment and suppressed interfacial recombination obtained with the CeO_x layer insertion.

As previously reported, PSCs based on TiO_2 ETLs suffer light-induced degradation due to the photocatalytic activity of TiO_2 [26,44]. Fig. 6 shows the normalized PCE decay of PSCs based on the TiO_2 and TiO_2/CeO_x ETLs as a function of storage time under 1 sun illumination. The PSCs based on the TiO_2/CeO_x ETL exhibited an outstanding light stability, maintaining over 88% initial PCE value after being aged for 300 min. By contrast, the PSCs based on the TiO_2 ETL almost failed after being aged for the same duration [28]. We speculate that the enhanced light stability is a result of two aspects. On the one hand, the presence of the CeO_x interlayer prevents the TiO_2 layer from directly contacting the perovskite layer, reducing the problem of photodegradation. On the other hand, the weakening of the device interface recombination contributes to the improvement of stability. It is important to note that a defective (oxygen-deficient) TiO_2 ETL was reported to improve the PCE and stability of PSCs owing to an unexpectedly large photoconductive gain and reduced ultraviolet photocatalytic activity [45]. Therefore, the effect of oxygen vacancy on device stability cannot be ruled out.

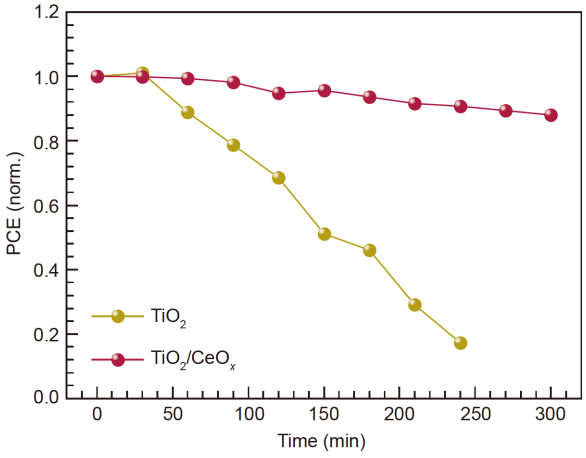

Figure 6 Normalized PCE decay of the unencapsulated PSCs based on the TiO_2 and TiO_2/CeO_x ETLs as a function of the storage time under 100 mW cm^{-2} irradiation (ambient air).

CONCLUSIONS

In summary, we demonstrated that the interfacial recombination losses of PSCs based on low-temperature-processed TiO_2 can be significantly reduced with introduction of a CeO_x interlayer. The introduction of CeO_x creates a cascade pathway for electron transport so that photogenerated electrons in the conduction band of $MAPbI_3$ can cascade into TiO_2 *via* CeO_x. This optimally positioned band alignment facilitates the extraction of electrons from the perovskite and their subsequent injection into TiO_2. Moreover, CeO_x suppresses the electrons' back transfer from TiO_2 to the perovskite due to the energy barrier at the TiO_2/CeO_x interface. This can effectively block interfacial charge recombination, leading to an increase in the quasi-Fermi level for electrons and an enhancement of the V_{oc}. As a result, the TiO_2/CeO_x-based device exhibits a maximum V_{oc} of 1.13 V with 300-mV potential loss compared with the TiO_2-based control device (1.08 V and 520 mV). The enhancement of V_{oc}, together with the increase in FF (from ~74% to ~76%), enables a PCE improvement from ~18% to more than 20%. These results suggest that designing an adequate band alignment is an effective way to reduce interfacial charge recombination and further improve the device

performance of PSCs.

Received 12 November 2020; accepted 22 January 2021; published online 2 April 2021

1 Kim JY, Lee JW, Jung HS, *et al.* High-efficiency perovskite solar cells. Chem Rev, 2020, 120: 7867–7918
2 Jena AK, Kulkarni A, Miyasaka T. Halide perovskite photovoltaics: Background, status, and future prospects. Chem Rev, 2019, 119: 3036–3103
3 Shi X, Chen J, Wu Y, *et al.* Efficient formamidinium-based planar perovskite solar cells fabricated through a CaI_2–PbI_2 precursor. ACS Sustain Chem Eng, 2020, 8: 4267–4275
4 Ma S, Cai M, Cheng T, *et al.* Two-dimensional organic-inorganic hybrid perovskite: From material properties to device applications. Sci China Mater, 2018, 61: 1257–1277
5 Shi P, Ding Y, Liu C, *et al.* Advanced partial nucleation for single-phase $FA_{0.92}MA_{0.08}PbI_3$-based high-efficiency perovskite solar cells. Sci China Mater, 2019, 62: 1846–1856
6 Https://www.Nrel.Gov/pv/assets/pdfs/best-research-cell-efficiencies.20200925.Pdf
7 Tress W. Perovskite solar cells on the way to their radiative efficiency limit—insights into a success story of high open-circuit voltage and low recombination. Adv Energy Mater, 2017, 7: 1602358
8 Stolterfoht M, Wolff CM, Márquez JA, *et al.* Visualization and suppression of interfacial recombination for high-efficiency large-area pin perovskite solar cells. Nat Energy, 2018, 3: 847–854
9 Stolterfoht M, Caprioglio P, Wolff CM, *et al.* The impact of energy alignment and interfacial recombination on the internal and external open-circuit voltage of perovskite solar cells. Energy Environ Sci, 2019, 12: 2778–2788
10 Wolff CM, Caprioglio P, Stolterfoht M, *et al.* Nonradiative recombination in perovskite solar cells: The role of interfaces. Adv Mater, 2019, 31: 1902762
11 Rajagopal A, Yao K, Jen AKY. Toward perovskite solar cell commercialization: A perspective and research roadmap based on interfacial engineering. Adv Mater, 2018, 30: 1800455
12 Shi X, Chen R, Jiang T, *et al.* Regulation of interfacial charge transfer and recombination for efficient planar perovskite solar cells. Sol RRL, 2020, 4: 1900198
13 Chen J, Park NG. Materials and methods for interface engineering toward stable and efficient perovskite solar cells. ACS Energy Lett, 2020, 5: 2742–2786
14 Choi K, Choi H, Min J, *et al.* A short review on interface engineering of perovskite solar cells: A self-assembled monolayer and its roles. Sol RRL, 2020, 4: 1900251
15 Qiu J, Yang S. Material and interface engineering for high-performance perovskite solar cells: A personal journey and perspective. Chem Rec, 2020, 20: 209–229
16 Mingorance A, Xie H, Kim H-, *et al.* Interfacial engineering of metal oxides for highly stable halide perovskite solar cells. Adv Mater Interfaces, 2018, 5: 1800367
17 Wang J, Liu Y, Chen X, *et al.* Functional metal oxides in perovskite solar cells. ChemPhysChem, 2019, 20: 2580–2586
18 Shin SS, Lee SJ, Seok SI. Metal oxide charge transport layers for efficient and stable perovskite solar cells. Adv Funct Mater, 2019, 29: 1900455
19 Haque MA, Sheikh AD, Guan X, *et al.* Metal oxides as efficient charge transporters in perovskite solar cells. Adv Energy Mater, 2017, 7: 1602803
20 Zhou Y, Li X, Lin H. To be higher and stronger—metal oxide electron transport materials for perovskite solar cells. Small, 2020, 16: 1902579
21 Xu X, Zhang H, Shi J, *et al.* Highly efficient planar perovskite solar cells with a TiO_2/ZnO electron transport bilayer. J Mater Chem A, 2015, 3: 19288–19293
22 Xu J, Fang M, Chen J, *et al.* ZnO-assisted growth of CH_3NH_3-$PbI_{3-x}Cl_x$ film and efficient planar perovskite solar cells with a TiO_2/ZnO/C_{60} electron transport trilayer. ACS Appl Mater Interfaces, 2018, 10: 20578–20590
23 Zhang P, Wu J, Zhang T, *et al.* Perovskite solar cells with ZnO electron-transporting materials. Adv Mater, 2018, 30: 1703737
24 Li N, Yan J, Ai Y, *et al.* A low-temperature TiO_2/SnO_2 electron transport layer for high-performance planar perovskite solar cells. Sci China Mater, 2020, 63: 207–215
25 Tavakoli MM, Yadav P, Tavakoli R, *et al.* Surface engineering of TiO_2 ETL for highly efficient and hysteresis-less planar perovskite solar cell (21.4%) with enhanced open-circuit voltage and stability. Adv Energy Mater, 2018, 8: 1800794
26 Leijtens T, Eperon GE, Pathak S, *et al.* Overcoming ultraviolet light instability of sensitized TiO_2 with meso-superstructured organometal tri-halide perovskite solar cells. Nat Commun, 2013, 4: 2885
27 Tan H, Jain A, Voznyy O, *et al.* Efficient and stable solution-processed planar perovskite solar cells *via* contact passivation. Science, 2017, 355: 722–726
28 Wang X, Deng LL, Wang LY, *et al.* Cerium oxide standing out as an electron transport layer for efficient and stable perovskite solar cells processed at low temperature. J Mater Chem A, 2017, 5: 1706–1712
29 Shi X, Wu Y, Chen J, *et al.* Thermally stable perovskite solar cells with efficiency over 21% *via* a bifunctional additive. J Mater Chem A, 2020, 8: 7205–7213
30 Zhou Y, Perket JM, Zhou J. Growth of Pt nanoparticles on reducible CeO_2 (111) thin films: Effect of nanostructures and redox properties of ceria. J Phys Chem C, 2010, 114: 11853–11860
31 Hu T, Xiao S, Yang H, *et al.* Cerium oxide as an efficient electron extraction layer for p–i–n structured perovskite solar cells. Chem Commun, 2018, 54: 471–474
32 Artiglia L, Agnoli S. Cerium oxide nanostructures on titania: Effect of the structure and stoichiometry on the reactivity toward ethanol oxidation. J Phys Chem C, 2018, 122: 20809–20816
33 Luo S, Nguyen-Phan TD, Johnston-Peck AC, *et al.* Hierarchical heterogeneity at the CeO_x–TiO_2 interface: Electronic and geometric structural influence on the photocatalytic activity of oxide on oxide nanostructures. J Phys Chem C, 2015, 119: 2669–2679
34 Artiglia L, Agnoli S, Paganini MC, *et al.* TiO_2@CeO_x core–shell nanoparticles as artificial enzymes with peroxidase-like activity. ACS Appl Mater Interfaces, 2014, 6: 20130–20136
35 Klasen A, Baumli P, Sheng Q, *et al.* Removal of surface oxygen vacancies increases conductance through TiO_2 thin films for perovskite solar cells. J Phys Chem C, 2019, 123: 13458–13466
36 Wang B, Zhang M, Cui X, *et al.* Unconventional route to oxygen-vacancy-enabled highly efficient electron extraction and transport in perovskite solar cells. Angew Chem Int Ed, 2020, 59: 1611–1618
37 Shi X, Ding Y, Zhou S, *et al.* Enhanced interfacial binding and electron extraction using boron-doped TiO_2 for highly efficient hysteresis-free perovskite solar cells. Adv Sci, 2019, 6: 1901213
38 Caprioglio P, Stolterfoht M, Wolff CM, *et al.* On the relation between the open-circuit voltage and quasi-Fermi level splitting in

efficient perovskite solar cells. Adv Energy Mater, 2019, 9: 1901631
39 Qi B, Wang J. Open-circuit voltage in organic solar cells. J Mater Chem, 2012, 22: 24315–24325
40 You J, Yang YM, Hong Z, *et al.* Moisture assisted perovskite film growth for high performance solar cells. Appl Phys Lett, 2014, 105: 183902
41 Shi J, Dong J, Lv S, *et al.* Hole-conductor-free perovskite organic lead iodide heterojunction thin-film solar cells: High efficiency and junction property. Appl Phys Lett, 2014, 104: 063901
42 Koster LJA, Mihailetchi VD, Ramaker R, *et al.* Light intensity dependence of open-circuit voltage of polymer:fullerene solar cells. Appl Phys Lett, 2005, 86: 123509
43 Bertoluzzi L, Sanchez RS, Liu L, *et al.* Cooperative kinetics of depolarization in $CH_3NH_3PbI_3$ perovskite solar cells. Energy Environ Sci, 2015, 8: 910–915
44 Chen TP, Lin CW, Li SS, *et al.* Self-assembly atomic stacking transport layer of 2D layered titania for perovskite solar cells with extended UV stability. Adv Energy Mater, 2018, 8: 1701722
45 Li Y, Cooper JK, Liu W, *et al.* Defective TiO_2 with high photoconductive gain for efficient and stable planar heterojunction perovskite solar cells. Nat Commun, 2016, 7: 12446

Acknowledgements This work was supported by the National Key Research and Development Program of China (2018YFB1500101), the 111 Project (B16016), the National Natural Science Foundation of China (U1705256, 51702096 and 61904053), and the Fundamental Research Funds for the Central Universities (2019MS026, 2019MS027 and 2020MS080).

Author contributions Dai S and Cai M supervised the project. Shi X conceived the original concept, designed the experiments, and wrote the manuscript. Shi X, Tao Y, and Li Z fabricated the devices and conducted the characterization and analysis with support from Peng H. Zhang Z provided helpful discussion during the revision process. Cai M and Liu X revised the manuscript, and all authors contributed to the general discussion.

Conflict of interest The authors declare no conflict of interest.

Supplementary information Experimental details and supporting data are available in the online version of the paper.

Xiaoqiang Shi obtained his BS and PhD degrees from North China Electric Power University in 2015 and 2020, respectively. He is currently a postdoctoral researcher at the College of Physics and Optoelectronic Engineering, Shenzhen University. His research interests include perovskite solar cells and antimony chalcogenide solar cells.

Molang Cai obtained her PhD degree from the Institute of Plasma Physics, Chinese Academy of Sciences in 2013. From 2013 to 2018, she successively worked as postdoctoral researcher at Queensland University of Technology and the National Institute of Materials Science, studying on efficient perovskite solar cells. In 2018, she joined North China Electric Power University as a professor. Her research interests mainly focus on efficient perovskite solar cells and *in-situ* measurement of photovoltaic materials and devices.

Songyuan Dai obtained his BS degree from Anhui Normal University in 1987, and MS and PhD degrees from the Institute of Plasma Physics, Chinese Academy of Sciences in 1991 and 2001, respectively. In 2012, he joined North China Electric Power University as a full professor. His research interests include dye-sensitized solar cells, quantum-dot solar cells and perovskite solar cells.

基于CeO_x修饰层降低界面复合损耗的光稳定钙钛矿太阳电池

时小强[1], 陶冶[1], 李卓芯[1], 彭会荣[1], 蔡墨朗[1,2*], 刘雪朋[1], 张中艳[1], 戴松元[1,2*]

摘要 尽管已经获得了很高的能量转换效率, 但由于非辐射复合损失, 钙钛矿太阳电池的潜力仍未完全释放. 钙钛矿层和电荷传输层之间的界面是发生复合损耗最多的地方. 对于低温制备的TiO_2电子传输层, 其与钙钛矿层之间的界面接触和能带对准对于非辐射复合损耗的减少来说至关重要. 在这项研究中, 我们利用CeO_x中间层修饰钙钛矿/TiO_2界面, 并研究了器件的电荷传输性能. 双层结构的TiO_2/CeO_x电子传输层改善了界面接触和能级匹配, 提高了电子转移, 抑制了界面复合. 基于TiO_2/CeO_x电子传输层的器件表现出1.13 V的高开路电压和超过20%的光电转换效率, 而基于TiO_2电子传输层器件的开路电压仅为1.08 V, 转换效率约为18%. 此外, 基于TiO_2/CeO_x电子传输层的钙钛矿器件在300 min光照后仍能保持初始效率的88%, 而基于TiO_2电子传输层的器件几乎失效. 这项研究为基于低温TiO_2电子传输层的钙钛矿太阳电池提供了一种增强转换效率和光稳定性的有效策略.

